

QCD equation of state and thermodynamic observables from computationally minimal Dyson-Schwinger equations

Yi Lu^{1,*}, Fei Gao^{2,†}, Yu-xin Liu^{1,3,4,‡} and Jan M. Pawłowski^{5,6,§}

¹*Department of Physics and State Key Laboratory of Nuclear Physics and Technology, Peking University, Beijing 100871, China*

²*School of Physics, Beijing Institute of Technology, 100081 Beijing, China*

³*Center for High Energy Physics, Peking University, 100871 Beijing, China*

⁴*Collaborative Innovation Center of Quantum Matter, Beijing 100871, China*

⁵*Institut für Theoretische Physik, Universität Heidelberg, Philosophenweg 16, 69120 Heidelberg, Germany*

⁶*ExtreMe Matter Institute EMMI, GSI, Planckstraße 64291 Darmstadt, Germany*



(Received 4 November 2023; accepted 16 June 2024; published 22 July 2024)

We study the QCD equation of state and other thermodynamic observables including the isentropic trajectories and the speed of sound. These observables are of eminent importance for the understanding of experimental results in heavy ion collisions and also provide a QCD input for studies of the timeline of heavy-ion-collisions with hydrodynamical simulations. They can be derived from the quark propagator whose gap equation is solved within a minimal approximation to the Dyson-Schwinger equations (DSEs) of QCD at finite temperature and density. This minimal approximation aims at a combination of computational efficiency and simplification of the truncation scheme while maintaining quantitative precision. This minimal DSE scheme is confronted and benchmarked with results for correlation functions and observables from lattice QCD at vanishing density and quantitative functional approaches at finite density.

DOI: [10.1103/PhysRevD.110.014036](https://doi.org/10.1103/PhysRevD.110.014036)

I. INTRODUCTION

The thermodynamic properties of strong interaction matter are of both experimental and theoretical interest. The phase structure of strongly interacting matter is explored in currently running and planned heavy-ion-collision facilities such as the BNL Relativistic Heavy Ion Collider (RHIC), GSI Facility for Antiproton and Ion Research (FAIR), JINR Nuclotron-based Ion Collider facility (NICA), and High Intensity heavy ion Accelerator Facility (HIAF). Its thermodynamic properties in the phase structure are governed by the QCD equation of state (EOS), i.e., thermodynamic functions such as pressure, entropy density, energy density, etc., at finite temperature T and quark chemical potential μ_q [1–4]. Specifically, for hydrodynamic simulations of heavy-ion collision, the QCD EOS is a crucial input as are further transport coefficients, see, e.g., [5,6].

Moreover, at large densities and small temperatures, the QCD EOS is required for explaining the physics of compact stars such as neutron stars, e.g., [7].

Accordingly, obtaining the EOSs and other thermodynamic observables from first principles QCD is of utmost importance for the physics phenomena discussed above. At finite chemical potential and in particular for $\mu_B/T \gtrsim 3$, these results can only be obtained with functional QCD approaches such as Dyson-Schwinger equations (DSEs) and the functional renormalization group (fRG) approach, as lattice simulations at finite chemical potential to date suffer from the sign problem. Investigations of the phase structure of QCD with functional QCD approaches have made significant progress over the past decade, see in particular [8–12], and the reviews [13] (DSE) and [14,15] (fRG). In turn, at vanishing μ_B , first principles QCD computations on the lattice provide benchmark results for the chiral phase transition temperature, thermodynamic observables, and fluctuations of conserved charges of QCD, see, e.g., [16–18], which also can be used for extrapolations to finite chemical potential [19–21].

By now the results for the chiral phase structure from functional approaches are converging quantitatively at finite density with the increasing order of the truncations used. Moreover, these up-to-date results meet the lattice benchmark results at vanishing (and low) chemical potential, see [11,12,22,23]. The convergent results include an estimate for an onset regime of new physics, potentially a critical

*Contact author: qwertylou@pku.edu.cn

†Contact author: fei.gao@bit.edu.cn

‡Contact author: yxliu@pku.edu.cn

§Contact author: J.Pawlowski@thphys.uni-heidelberg.de

Published by the American Physical Society under the terms of the [Creative Commons Attribution 4.0 International license](https://creativecommons.org/licenses/by/4.0/). Further distribution of this work must maintain attribution to the author(s) and the published article's title, journal citation, and DOI. Funded by SCOAP³.

end point (CEP), at about $(T, \mu_B) \sim (110, 600)$ MeV. This location lies beyond the quantitative convergence regime $\mu_B/T \lesssim 4$ of the current best approximations, and hence it is only an estimate and not a fully quantitative prediction. Still, this is exciting news and furthermore there is an ongoing quest for even more elaborate truncations that aim for full apparent convergence. However, the present approximations already allow for quantitative computation in the regime $\mu_B/T \lesssim 4$ and for estimates in the regime $\mu_B/T \gtrsim 4$.

This opens the path towards a comprehensive analysis of the equation of state, further thermodynamic observables, fluctuations of conserved charges, as well as timelike observables such as transport coefficients within functional approaches. In the present work we contribute twofold to this endeavor.

(i) We want to make quantitative functional QCD computations accessible to a wider audience beyond the technical experts. To that end we set up a minimal computational scheme for DSE computation: such a scheme aims at the technically most simple approximation at finite temperature and density that still reproduces the phase structure results with the state-of-the-art approximation scheme in [11,12,22,23] and, hence, allows a relatively simple access to many observables beyond the phase structure itself.

(ii) We compute the equation of state and other thermodynamic observables in a wide range of T and μ_B within this scheme. This allows us to study further thermodynamic observables such as the isentropic trajectories and the speed of sound, highly relevant for hydrodynamic simulations at finite density.

This work is organized as follows: In Sec. II, we present the framework of the minimal scheme and its agreement with the other studies in vacuum. In Sec. III, we apply the framework in the plane of temperature and chemical potential and obtain the chiral phase transition. Then in Sec. IV, we present the results of EOS in the (μ, T) plane and also the isentropic trajectories. In Sec. V, we summarize the main results and make further discussions and outlook.

II. THE MINIMAL DSE SCHEME

In this section we develop the minimal truncation scheme for the DSE approach at finite temperature and density, which can provide quantitative and semiquantitative results with minimal computational effort (miniDSE). A central element of the system of DSEs in QCD at finite temperature and density is the DSE or gap equation for the quark propagator. The full quark propagator at finite density and temperature provides access to many observables, ranging from the chiral phase boundary over the density to fluctuations of conserved charges. We use it here also for illustrative purposes. The quark DSE is given by

$$[S(p)]^{-1} = [S_0(p)]^{-1} + \Sigma_0(p), \quad (1a)$$

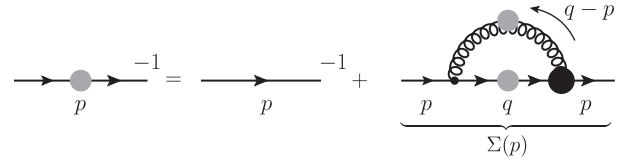


FIG. 1. Quark DSE for the quark self-energy $\Sigma(p)$. Full propagators are depicted with lines with gray blobs, the full vertex is depicted with black blob, and the classical vertex with small black dot. The classical quark propagator is depicted with a straight black line.

where S_0 is the classical bare propagator,

$$S_0(p) = \frac{1}{i\not{p} + m}, \quad (1b)$$

where m is the matrix of current quark masses with entries m_f for all flavors $f = 1, \dots, N_f$. Σ_0 is the bare self-energy, which satisfies the DSE

$$\Sigma_0(p) \simeq \frac{4}{3} g_s \int \frac{d^4 q}{(2\pi)^4} \gamma_\mu S(q) \Gamma_\nu(q, p) D_{\mu\nu}(k). \quad (1c)$$

In (1) we have dropped the renormalization details for the sake of structural simplicity. We shall use a Bogoliubov-Parasiuk-Hepp-Zimmermann (BPHZ)-type renormalization procedure setup in [24], which features renormalization constants, which are set to unity for a sufficiently large renormalization group scale. More details are provided in Sec. II B. In Eq. (1c), $D_{\mu\nu}(k)$ is the full gluon propagator with gluon momenta $k = q - p$, and Γ_ν is the full quark-gluon vertex. The diagrammatic depiction of (1) is provided in Fig. 1 and the momentum arguments in the quark-gluon vertex are the incoming and outgoing quark momenta. We proceed with the detailed discussion of the miniDSE scheme: In Sec. II A we put forward the essential elements for such a minimal scheme in functional approaches. Then, in Sec. II B the scheme is developed and its application is illustrated a quantitative analysis of vacuum QCD. Finally, in Sec. II D we demonstrate the remaining developments at finite temperature and density, which then completes the whole scheme used in the present work.

A. Minimal scheme for functional approaches

The minimal scheme in functional approaches (miniDSE or miniFRG) supposedly allows for quantitative results with a small systematic error, while minimizing or reducing the computational costs. It builds on previous developments in [11,22] and is built on two pillars.

(i) *Minimal fluctuations.* It is an advantageous property of functional approaches such as the DSE and the fRG, that QCD correlation functions such as continuum extrapolated lattice results or quantitative functional QCD results can be implemented straightforwardly. Moreover, functional loop

equations of QCD for given external parameters such as temperature T , baryon chemical potential μ_B , and number of quark flavors N_f can be expanded about QCD for different external parameters; for more details see [12,22]. This minimizes the amount of quantum, thermal, and density fluctuations carried by the functional equations themselves. The benefit of such a procedure is twofold: First, assuming a negligible or small systematic error of the input it minimizes the systematic error as the latter only concerns the fluctuations carried by the functional equations. This allows us to reduce the intricacy of the approximation within the DSE or fRG considerably without a significant loss of the quantitative nature of the result. Second, it minimizes the need of renormalizing the functional equations. For a given n -point correlation function $\Gamma^{(n)}$, the procedure can be expressed as follows [12]:

$$\Gamma_{\mathbf{v}}^{(n)} = \Gamma_{\mathbf{v}_0}^{(n)} + \Delta\Gamma_{\mathbf{v},\mathbf{v}_0}^{(n)}, \quad (2)$$

where \mathbf{v} collects the external parameters, e.g., $\mathbf{v} = (T, \mu_B, N_f, m_f)$. Equation (2) represents the difference of the DSEs between \mathbf{v} and \mathbf{v}_0 and constitutes a functional equation for $\Gamma_{\mathbf{v}}^{(n)}$ with the input $\Gamma_{\mathbf{v}_0}^{(n)}$. We emphasize that the difference DSE in Eq. (2) depends on further $\Gamma_{\mathbf{v}}^{(n)}$, which are computed from their own difference DSEs.

An instructive example is the quark gap equation at finite temperature and chemical potential which can be expanded about the vacuum results from other studies,

$$\Sigma_{\mathbf{v}} = \Sigma_{\mathbf{v}_0} + \Delta\Sigma_{\mathbf{v},\mathbf{v}_0}, \quad (3)$$

where $\mathbf{v} = (T, \mu_B, N_f, m_f)$ and $\mathbf{v}_0 = (0, 0, N_f, m_f)$ and the input, e.g., is the quark propagator and vertices from the quantitative DSE study of vacuum QCD in [24]. Then, the gap equation Eq. (3) can be resolved for $\Delta\Sigma$ with the input of the vacuum self-energy $\Sigma_{\mathbf{v}_0}$, the vacuum quark-gluon vertex $\Gamma_{\mu,\mathbf{v}_0}$ and the vacuum gluon propagator $D_{\mu\nu,\mathbf{v}_0}$. This leads us to

$$\Delta\Sigma(p) \simeq \frac{4}{3}g_s \left\{ \sum_q \gamma_\mu S_{\mathbf{v}}(q) \Gamma_{\nu;\mathbf{v}}(q,p) D_{\mu\nu;\mathbf{v}}(k) - \int_q \gamma_\mu S_{\mathbf{v}_0}(q) \Gamma_{\nu;\mathbf{v}_0}(q,p) D_{\mu\nu;\mathbf{v}_0}(k) \right\}, \quad (4)$$

where \int is the momentum integration in the vacuum and \sum takes into account a Matsubara sum for $T \neq 0$,

$$\sum_q = T \sum_{n \in \mathbb{Z}} \int \frac{d^3 q}{(2\pi)^3}, \quad \int_q = \int \frac{d^4 q}{(2\pi)^4}. \quad (5)$$

Note that the solution of the gap equation Eq. (4) requires the knowledge of the vertex and the gluon propagator,

which satisfy their respective difference version of the DSE Eq. (2).

For numerical convenience it is advisable to recast the right-hand side of Eq. (4) such that the exponential suppression of thermal contributions is included not by differences of sums and integrals, for a detailed discussion see [22]. There, this has been explained at the example of the gluon propagator. For the quark gap equation, the sums and integrals on the right-hand side of Eq. (4),

$$\Delta\Sigma(p) \simeq \frac{4}{3}g_s \left\{ \sum_q \left[\gamma_\mu S_{\mathbf{v}} \Gamma_{\nu;\mathbf{v}} D_{\mu\nu;\mathbf{v}} - \gamma_\mu S_{\mathbf{v}_0} \Gamma_{\nu;\mathbf{v}_0} D_{\mu\nu;\mathbf{v}_0} \right] + \left[\sum_q - \int_q \right] \gamma_\mu S_{\mathbf{v}_0} \Gamma_{\nu;\mathbf{v}_0} D_{\mu\nu;\mathbf{v}_0} \right\}. \quad (6)$$

To begin with, the DSE for $\Delta\Sigma$ is finite (for fixed N_f and m_f); the subtractions from the renormalization have dropped out. Moreover, the second line only depends on the input, both the thermal sum and the integral have the same summand/integrand. Then, the thermal suppression is readily extracted in a numerically safe way. Note that the second line can be precompiled for all \mathbf{v} and serves as an input in the first line. Moreover, in most cases the second line carries most of the thermal change. If solving the set of DSEs in an iterative procedure about $\Delta\Gamma^{(n)} = 0$, the difference of the self-energies $\Delta\Sigma$ in the first iteration step is simply given by the second line. As this carries already the correct thermal suppression, it is also present in the first line due to the subtraction of the summands/integrands. In conclusion, this leads us to a numerically stable and cost-efficient procedure for solving DSEs.

(ii) *Minimal correlation functions.* Complete n -point correlation functions $\Gamma^{(n)}(p_1, \dots, p_n)$ carry a rapidly increasing number of tensor structures as

$$\Gamma^{(n)}(p_1, \dots, p_n) = \sum_i \lambda^i(p_1, \dots, p_{n-1}) T^i. \quad (7)$$

Their respective scalar dressing functions λ^i depend on the momenta p_1, \dots, p_{n-1} , the remaining momentum p_n is fixed by momentum conservation. However, only few of these dressings have a sizable impact within the system of functional equations and higher order vertices are typically suppressed due to space-time and momentum locality of the vertices in gauge-fixed QCD; for more details see [14].

In our example of the difference gap equation for Eq. (3), a respective evaluation concerns only the quark-gluon vertex Γ_μ . In the vacuum it has a basis of twelve tensor structures that come with respective dressings,

$$\Gamma_\mu(q, p) = \sum_{i=1}^{12} \mathcal{T}_\mu^{(i)}(q, p) \lambda^{(i)}(q, p), \quad (8)$$

while its transverse part carries a basis of eight tensor structures and one typically simply considers transverse projections of eight elements; see, for example, [24]. There it has been shown in detail, that only three of these eight tensors are relevant, say 1, 4, and 7, and the other tensors can be dropped completely even for quantitative purposes. This leads us to a reduced vertex,

$$\Gamma_\mu^{\text{red}}(q, p) = \sum_{i=1,4,7} \mathcal{T}_\mu^{(i)}(q, p) \lambda^{(i)}(q, p), \quad (9)$$

which is used in combination with the gap equation for the quarks, Eq. (1c), and gluons as well as with the DSE for the gluonic vertices. Similarly to Eq. (3), the vertex DSEs are expanded about the quantitative vacuum solution, taken, e.g., from [24],

$$\Delta\Gamma_{\mu;v,v_0} = \Gamma_{\mu;v} - \Gamma_{\mu;v_0}. \quad (10)$$

Equation (10) is expanded analogously to Eq. (8) in terms of sums and integrals. As there this leads to numerically stable and rapidly converging iterations in the DSE.

In summary, the above minimal scheme allows us to obtain quantitatively reliable results for observables with a significant reduction of the numerical costs and a sizable improvement of the stability of the convergence of the numerics. In combinations this can lead to a reduction of the computation time by orders of magnitude. Moreover, some of these reduced truncations in the miniDSE are easily accessible technically also for nonexperts.

B. miniDSE scheme in the vacuum

In this section we develop the minimal truncation scheme for the DSE approach (miniDSE) in the vacuum. The key to this approach is the quantitative solution of the quark gap equation or quark DSE for the full quark propagator $S(p)$ already discussed in the introduction of Sec. II, see (1). Its renormalized form is given by

$$[S(p)]^{-1} = i\not{p} + m + \Sigma(p), \quad (11)$$

with the renormalized mass m and the renormalized self-energy Σ . The latter satisfies the renormalization conditions

$$\text{tr}_D \Sigma(p) \Big|_{p^2=\mu^2} = 0, \quad \text{tr}_D \frac{\not{p}}{p^2} \Sigma(p) \Big|_{p^2=\mu^2} = 0, \quad (12)$$

with the renormalization scale μ^2 . The first condition entails that the renormalized mass m_q is the full mass function at $p^2 = \mu^2$, while the second condition entails that the wave function of the quark is trivial at $p^2 = \mu^2$. The conditions Eq. (12) can be summarized in

$$\Sigma(p) \Big|_{p^2=\mu^2} = 0. \quad (13)$$

Similar renormalization conditions hold for the corrections of the ghost and gluon propagators, as well as the primitively divergent three- and four-point vertices at the symmetric point,

$$\bar{p}^2 = p_i^2 = \mu^2, \quad i = 1, \dots, n, \quad (14)$$

with $n = 3, 4$ for the three- and four-gluon, ghost-gluon, and quark-gluon vertices. It is left to detail the renormalization scheme used here. Instead of using the usual MOM scheme with multiplicative renormalization, the numerical computation will be performed with the MOM² scheme devised in [24], briefly recapitulated below.

1. Renormalization

Equation (11) is computed within the MOM² scheme developed in [12,22,24] that also underlies the fRG computations. It is for the latter reason that this scheme allows the direct insertion of fRG results, as well as DSE results computed in this scheme. We refer to [24] for a detailed analysis of this renormalization group (RG) scheme in the vacuum: Its chiefly important property is the fact that its renormalization factors converge towards unity for sufficiently large renormalization scales $\mu/\Lambda_{\text{QCD}} \gg 1$; typically one uses $\mu \gtrsim \mathcal{O}(10)$ GeV. This convergence to unity is a property of the RG scheme used in the fRG approach, which is a generalized BPHZ subtraction scheme. It is precisely this property that allows for a direct use of fRG input, and is achieved by appropriate self-consistent subtractions at the renormalization point μ .

We illustrate the practical implementation of the subtraction scheme at the example of the quark gap equation (1c), the other subtractions are implemented similarly. The BPHZ-type subtractions in [24] are simply given by the DSEs for a theory with a sharp infrared momentum cutoff Λ in the propagators, leading to

$$G_\Lambda(p^2 \leq \Lambda^2) = 0, \quad (15)$$

for quark, gluon, and ghost propagators. For the specific scheme used here we employ cutoffs $\Lambda \gg \Lambda_{\text{QCD}}$ and set the RG scale $\mu = \Lambda$. Then, the propagator G_Λ shows the standard perturbative behavior for $p \geq \Lambda$. Accordingly, the difference between the full propagator and the infrared regularized one vanished approximately up to higher order terms, namely,

$$[G - G_\Lambda](p^2 \gtrsim \mu^2) \approx 0, \quad [G - G_\Lambda](p^2 < \mu^2) = G(p). \quad (16)$$

In summary this leads us to

$$\Sigma(p) = \Delta\Sigma_\Lambda(p) + \text{loops}_\Lambda(p), \quad (17)$$

where $\text{loops}_\Lambda(p)$ is simply the difference of the loop in (1c) with the full propagators and vertices and the loop with infrared regularized propagators G_Λ and the respective vertices. $\Delta\Sigma_\Lambda$ carries the renormalization condition and renders the sum on the right-hand side of Eq. (17) Λ independent. Effectively this reduces to the self-energy loop in (1c) with the propagators

$$G(p)\theta(\Lambda^2 - p^2), \quad (18)$$

where we have dropped subleading terms that vanish with $\Lambda \rightarrow \infty$. At the renormalization point $\bar{p}^2 = \mu^2 = \Lambda^2$ the self-energy vanishes, Eq. Eq. (13), which fixes $\Delta\Sigma_\Lambda(p)$,

$$\Delta\Sigma_\Lambda(p) = -\frac{1}{4}\text{tr}_D \text{loops}_\Lambda(p) \Big|_{p^2=\mu^2} - \not{p} \frac{1}{4}\text{tr}_D \left[\frac{\not{p}}{p^2} \text{loops}_\Lambda(p) \right]_{p^2=\mu^2}, \quad (19)$$

where tr_D is the Dirac trace. This choice also removes the Λ dependence of the self-energy up to subleading terms that vanish for $\Lambda \rightarrow \infty$. The first term in Eq. (19) is a finite mass renormalization, while the second term constitutes a finite wave function renormalization for the quark in the limit $\Lambda \rightarrow \infty$. This factor can be absorbed readily in the definition of the quark field. In summary, this leaves us with a trivial limit for all renormalization constants for $\Lambda/\Lambda_{\text{QCD}} \rightarrow \infty$. The derivation of Eq. (17) and (19) from the Wilsonian point of view including rules for its practical implementation can be found in Appendix A in [24].

Finally, we note that the classical quark propagator $S_0(p)$ in (1b) is flavor diagonal. The full quark-gluon vertex Γ_ν is also taken flavor diagonal, and hence (1c) constitutes equations for the self-energies Σ^f for a given flavor f , which only depends on the classical and full quark propagators S_0^f, S^f or rather Σ^f of the same flavor f and Γ_ν^f . Hence, the quark gap equation is flavor diagonal; however, the gluon propagator depends on all flavors.

2. Approximation

In the current work we restrict ourselves to 2 + 1 flavor QCD with $f = u, d, s$. In the vacuum, the full quark propagator is parametrized with a flavor diagonal Dirac dressing A and a scalar dressing B , namely,

$$S^{-1}(p) = i\not{p}A(p) + B(p). \quad (20)$$

The vacuum gluon propagator is transverse in the Landau gauge used in the current work and has the transverse dressing Z ,

$$D_{\mu\nu}(k) = G_A(k)\Pi_{\mu\nu}^\perp(k), \quad \Pi_{\mu\nu}^\perp(k) = \delta_{\mu\nu} - \frac{k_\mu k_\nu}{k^2}, \quad (21)$$

with the transverse projection operator Π^\perp and the scalar propagator part,

$$G_A(k) = \frac{Z(k)}{k^2}, \quad (22)$$

with $Z(k)$ the dressing function. By now, the vacuum gluon propagator Eq. (21) can be very accurately computed, e.g., for the 2 + 1 flavor gluon propagator, there are consistent results from lattice QCD simulations and functional computations [11,12,22,25,26]. Therefore, we use the parametrization of the 2 + 1 flavor gluon put forward in [24]; see Appendix A for the details.

The last ingredient is the quark-gluon vertex. As discussed before, the quark-gluon vertex in the vacuum has a complete basis of twelve tensor structures, $\{\mathcal{T}^{(i)}\}$ with $i = 1, \dots, 12$, while its transverse part can be expanded in eight transverse projections of these tensors with $i = 1, \dots, 8$, see, e.g., [24]. For the development of our minimal truncation scheme we can build on many functional results obtained for the quark-gluon vertex in the vacuum, see, e.g., [24,27–33]. At finite temperature and density these transverse projections all come with a thermal split, which will be discussed later in Sec. IID.

The following construction of a simplified quark-gluon vertex in the miniDSE scheme builds on results of the in-detail analysis of the importance ordering of the vertices in [24] in the vacuum. Moreover, we also work in the information from DSE results at finite temperature and density obtained in the precursor of the present minimal scheme in [22], and its comparison with the full computation in [12]. This combined analysis showed that five of the eight tensor structures are completely subleading, and we only have to consider the transverse projections of the remaining three,

$$\begin{aligned} \mathcal{T}_\mu^{(1)}(q, p) &= -i\gamma_\mu, \\ \mathcal{T}_\mu^{(4)}(q, p) &= -i\sigma_{\mu\nu}k^\nu, \quad \sigma_{\mu\nu} = \frac{i}{2}[\gamma_\mu, \gamma_\nu], \\ \mathcal{T}_\mu^{(7)}(q, p) &= \frac{i}{3} \left\{ \sigma_{\alpha\beta}\gamma_\mu + \sigma_{\beta\mu}\gamma_\alpha + \sigma_{\mu\alpha}\gamma_\beta \right\} l^\alpha k^\beta. \end{aligned} \quad (23)$$

Each tensor comes with a momentum dependent dressing function $\lambda^{(i)}(q, p)$ with the incoming and outgoing quark momenta q and p , respectively, and the gluon momentum k and the weighted sum of the quark and antiquark momenta l ,

$$k = q - p, \quad l = \frac{1}{2}(q + p). \quad (24)$$

Then, the miniDSE quark-gluon vertex takes the form

$$\Gamma_\mu(q, p) = \sum_{1,4,7} \mathcal{T}_\mu^{(i)}(q, p)\lambda^{(i)}(q, p). \quad (25)$$

The terms in Eq. (25) have the following relevance ordering [24]: the by far dominant component of the vertex is that with the classical (chiral) tensor structure, $\mathcal{T}_1\lambda_1$, and the dressing is constrained by the Slavnov-Taylor identities (STIs). This is followed by the chiral symmetry breaking part $\mathcal{T}_4\lambda_4$. The smallest contribution originates in the second chirally symmetric part $\mathcal{T}_7\lambda_7$. The Dirac structures of quark-gluon vertex are adopted from [24], except \mathcal{T}_7 which has less overlap with the other components and avoids kinematic singularities due to its symmetric form, see [34].

Then, the fully quantitative miniDSE scheme would utilize the splits Eq. (2) with $\mathbf{v}' = (N'_f, m'_f, T', \mu'_B) = (N_f, m_f, 0, 0)$ or even with $T' = T$ as well as the quantitative data from [24] or finite temperature results. Moreover, at finite temperature and density the dressings $\lambda_{1,4,7}$ with or without thermal split would be approximated by combinations of the dressings of the quark propagator as done in [22]. The latter step further reduces the numerical costs significantly. The quantitative nature of this approximation has already been confirmed in [12,22]. This concludes our discussion of the quantitative miniDSE scheme for applications to the phase diagram of QCD.

C. Simplifications beyond the miniDSE scheme

In the present work we will further simplify the scheme by approximating the vertex dressings also at $T = 0$ with combinations of the propagator dressings. Moreover, we shall drop the least important part $\mathcal{T}_7\lambda_7$, even though it accounts for an about 20% decrease of the mass function. We accommodate for this decrease of the mass function by decreasing the coupling constant with roughly 3% compared with the full QCD coupling in [24]. A comparison of the λ_7 contribution on the quark mass function is shown in Fig. 2.

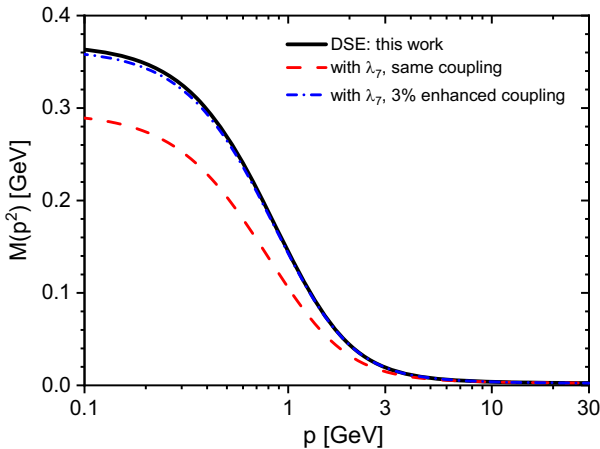


FIG. 2. Quark mass function $M(p^2) = B(p^2)/A(p^2)$ from the truncation scheme Eq. (26), compared to the scheme with an additional λ_7 structure from the data input of [24], and with the λ_7 and a 3% enhanced coupling.

In summary, this leads us to a computationally minimal scheme only in terms of the quark dressings with the quark gluon vertex,

$$\Gamma_\mu(q, p) = \mathcal{T}_\mu^{(1)}(q, p)\lambda^{(1)}(q, p) + \mathcal{T}_\mu^{(4)}(q, p)\lambda^{(4)}(q, p), \quad (26)$$

where the dressing of the classical tensor structure is constrained by the STIs for the quark-gluon vertex. We shall use

$$\lambda^{(1)}(q, p) = g_s F(k^2) \Sigma_A(q, p), \quad (27)$$

with the ghost dressing function $F(k^2) = k^2 G_c(k)$, where $G_c(k)\delta^{ab}$ is the ghost propagator. The other factor Σ is the sum of the quark dressings A defined in Eq. (20),

$$\Sigma_A(q, p) = \frac{A(p) + A(q)}{2}. \quad (28)$$

Several studies suggest that $\lambda^{(4)}$ is proportional to differences of the scalar quark dressing function [35–37],

$$\Delta_B(q, p) = \frac{B(p) - B(q)}{p^2 - q^2}. \quad (29)$$

The scalar dressing of the quark propagator carries the RG scaling of the quark and antiquark leg of the quark-gluon vertex. The RG scaling of any vertex dressing λ^i also has to accommodate the RG scaling of the gluon momentum as $\propto 1/Z^{1/2}(k)$, with the gluon dressing defined in Eq. (22). It has been shown in [22,24] by comparison to the full vertex computed in [24] (DSE) and fRG [31] (fRG), that this factor indeed not only carries the appropriate RG scaling but also the correct momentum dependence of λ_4 in the vacuum. For the explicit comparison, see, e.g., Fig. 15 in Ref. [22]. Hence, in the vacuum we choose

$$\lambda^{(4)}(q, p) = \frac{g_s}{Z^{1/2}(k)} \Delta_B(q, p), \quad (30)$$

with $Z(k)$ the gluon dressing function introduced in Eq. (21), see [22]. In the deep infrared, Eq. (30) introduces a kinematic singularity into the vertex that it absent in the direct computation. Note however that, in our computations, the vertex is always attached to a gluon propagator with momentum k and the factor $1/Z^{1/2}(k)$ is canceled. Moreover, the loop integration introduces a further k^2 at finite temperature and k^3 in the vacuum, which leads to a very efficient suppression of this regime. This is checked with a comparison to the results from computations with full vertices which allows for a systematic error estimate, which is described in detail in Appendix B. It is shown that

the change of results is no more than 3%, well within the systematic error estimate of our computation and hence supports our procedure.

This concludes the discussion of the simplified version of the miniDSE scheme in the quark sector used in the present paper. The price to pay for the last simplification steps Eq. (26)(30) beyond the miniDSE scheme is a loss of quantitative reliability for baryon chemical potentials with $\mu_B/T \gtrsim 3$. This will be discussed in detail in Sec. II D. The quantitative reliability regime for $\mu_B/T \lesssim 3$ has been checked with the results from the fully quantitative finite temperature and chemical potential computation in [12]: the loss of quantitative reliability manifests itself, e.g., in an increasing difference of the chiral phase transition line from that in full QCD in Fig. 6 for these chemical potentials including a 10% reduction of the temperature and the chemical potential values of the location of the critical end point from the estimated regime in full quantitative functional QCD. For the first computation of thermodynamic quantities we consider this an acceptable price to pay. Still, we emphasize that the lack of quantitative reliability from the simplified construction of λ_7 and λ_4 is highly relevant for self-consistency checks of functional approaches: a necessary condition for the full quantitative reliability or small systematic error bars is the confirmation of lattice and functional benchmarks at small chemical potentials without the need for phenomenological parameters such as a minor decrease of the coupling. Amongst other conditions, it is this property which informs the current quantitative reliability bound for predictions from functional QCD of $\mu_B/T \lesssim 4$.

The vertex dressings in Eq. (26)(30) are also based on dressings from the ghost-gluon sector. The ghost propagator is almost independent of temperature and density and we use the vacuum fRG data in two-flavor QCD [31]. See Appendix A for the details. In turn, the gluon dressings are computed from a difference DSE analogously to that of the quark discussed around Eq. (5). The respective difference DSE have been discussed in detail in [12,22]. This procedure accommodates further intricacies that arise from the need of a numerically optimal treatment of differences of frequency integrals and Matsubara sums, and hence we defer its description to the next section, Sec. IV, where the setup at finite T, μ_B is described, see Eqs. (42) to (45).

With this input and simplification of the miniDSE scheme, the quark propagators are computed in the isospin symmetry approximation with $m_u = m_d = m_l$ with the coupling parameters $\alpha_s = g_s^2/(4\pi)$, m_l, m_s being fixed at an RG scale $\mu = 15$ GeV. This is significantly lower than the perturbative RG scale $\mu = 40$ GeV used in [24] for precision computations in the vacuum, but suffices for the present accuracy goals. We use

$$\begin{aligned} \alpha_s &= 0.235, \\ m_l &= 3.0 \text{ MeV}, \quad m_s = 27m_l = 81 \text{ MeV}, \end{aligned} \quad (31)$$

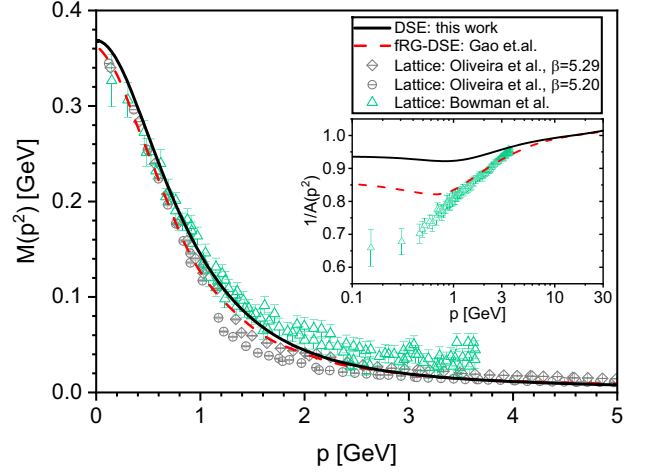


FIG. 3. Light (u, d) quark mass functions $M(p^2) = B(p^2)/A(p^2)$ and the wave function $1/A(p^2)$ calculated from the truncation scheme Eq. (26). The results from lattice QCD simulation [38] and previous DSE computation in the fully coupled scheme [24] are also shown for comparison.

at $\mu = 15$ GeV, which is compatible with the coupling parameters in [24] within the same RG scheme, the MOM^2 scheme.

As a benchmark result we show the light quark mass function $M(p^2) = B(p^2)/A(p^2)$ and the quark wave function $1/A(p^2)$ in Fig. 3 in comparison to the quantitative fRG-DSE results in [24] and the lattice results from [38]. From this quark propagator we compute the reduced quark condensate

$$\Delta_{l,s} = \langle \bar{q}q \rangle_l - \frac{m_l}{m_s} \langle \bar{q}q \rangle_s. \quad (32)$$

For the comparison with the lattice and functional results for the reduced condensate, we have to map our present results to the respective RG scales. This has been described in detail in [24] where the precision results for the quark condensates have been compared to the lattice results at the lattice RG scale $\mu_{\text{lat}} = 2$ GeV. Hence, we simply map the present result to the lattice RG scale and compare it with the lattice and functional results. We are led to

$$\Delta_{l,s}(\mu_{\text{lat}}) = -(277.6 \text{ MeV})^3. \quad (33)$$

Another and even more direct benchmark is provided with the light quark condensate in the chiral limit: it relates to the quark mass function [24,39,40], and we obtain

$$\Delta_{l,\chi}(\mu_{\text{lat}}) = -(273.9(8) \text{ MeV})^3, \quad (34)$$

in comparison with the functional precision result in the vacuum $\Delta_{l,\chi}(\mu_{\text{lat}}) = (269.3(7) \text{ MeV})^3$ [24] and the lattice result $\Delta_{l,\chi}(\mu_{\text{lat}}) = (272(5) \text{ MeV})^3$ (FLAG [41]). $\Delta_{l,\chi}$ can

also be used to determine the chiral condensate at the physical quark mass, and we find

$$\Delta_I(\mu_{\text{lat}}) = -(274.5 \text{ MeV})^3, \quad (35)$$

in comparison to the functional precision result $\Delta_I(\mu_{\text{lat}}) = (272.0 \text{ MeV})^3$ in [24].

Moreover, using the Pagels-Stokar formula [22] (PS), we obtain an estimate for the pion decay constant of $f_\pi = 94.7 \text{ MeV}$. Given the expected 10% deviation of the PS result from the full results, this agrees well with $f_\pi \approx 93 \text{ MeV}$. Moreover, the Gell-Mann–Oakes–Renner relation yields a pion mass of $m_\pi = 140.4 \text{ MeV}$.

In summary, despite its relative simplicity the quark propagator and the derived observables in the vacuum, obtained from the present approximation, show an already impressive agreement with the precision functional results and those from lattice simulations. We emphasize again that the truncation scheme with the simplifications Eq. (26) and (30) beyond the miniDSE scheme only requires a slight decrease of the coupling compared to the fully coupled DSE result [24]. At finite temperature and chemical potential, the scheme is quantitatively reliable up to $\mu_B/T \lesssim 3$, which will be seen in the following sections.

D. miniDSE scheme at finite T and μ_B

We proceed with a discussion of the extension of the miniDSE scheme to finite temperature and density. This concerns, in particular, the thermal split and the treatment of the gluon sector.

The full quark and gluon propagators $S(p)$ and $D_{\mu\nu}(p)$ at finite temperature and density are parametrized as follows:

$$\begin{aligned} S^{-1}(\tilde{p}) &= i\gamma_4 \tilde{\omega}_n C(\tilde{p}) + i\boldsymbol{\gamma} \cdot \mathbf{p} A(\tilde{p}) + B(\tilde{p}), \\ p^2 D_{\mu\nu}(p) &= \Pi_{\mu\nu}^E(p) Z_E(p) + \Pi_{\mu\nu}^M(p) Z_M(p), \end{aligned} \quad (36)$$

with

$$\tilde{\omega}_n = \omega_n + i\mu_q, \quad \tilde{p} = p + i\mu_q, \quad p = (\mathbf{p}, \omega_n), \quad (37)$$

and the quark and gluon Matsubara frequencies

$$\text{quark: } \omega_n = (2n + 1)\pi T, \quad \text{gluon: } \omega_n = 2n\pi T, \quad (38)$$

respectively. Equation (36) also depends on the electric and magnetic gluon projection operators $\Pi_{\mu\nu}^{E,M}$,

$$\begin{aligned} \Pi_{\mu\nu}^M(p) &= (1 - \delta_{\mu 4})(1 - \delta_{\nu 4}) \left(\delta_{\mu\nu} - \frac{p_\mu p_\nu}{p^2} \right), \\ \Pi_{\mu\nu}^E(p) &= \delta_{\mu\nu} - \frac{p_\mu p_\nu}{p^2} - \Pi_{\mu\nu}^M. \end{aligned} \quad (39)$$

The quark DSE at finite (T, μ_B) is of the form (1) with a spatial momentum integral and a thermal sum over Matsubara frequencies defined in Eq. (5). The DSE of

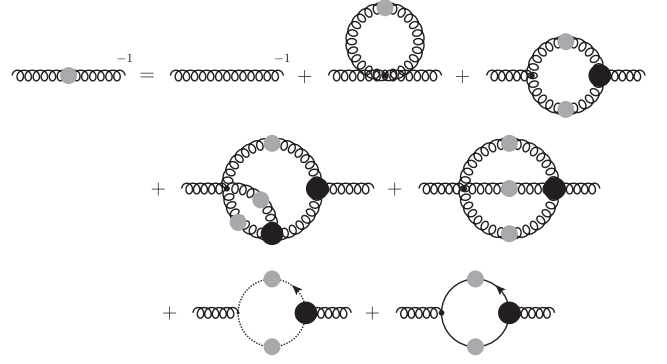


FIG. 4. Diagrammatic depiction of the gluon DSE. Full propagators are depicted with lines with gray blobs, full vertices are depicted with large black blobs, and classical vertices with small black dots. The classical gluon propagator is depicted with a spiralling black line.

the gluon propagator at finite T and quark chemical potentials (μ_u, μ_d, μ_s) is computed along the lines suggested in [22]. A diagrammatic depiction of the gluon DSE is provided in Fig. 4.

We first use the difference DSE for the gluon propagator as in Eq. (5) in an expansion about the gluon propagator in the vacuum,

$$D_{\mu\nu, \mathbf{v}}^{-1}(k) = D_{\mu\nu, \mathbf{v}_0}^{-1}(k) + \Delta\Pi_{A; \mu\nu}^{\mathbf{v}, \mathbf{v}_0}(k), \quad (40)$$

with

$$\mathbf{v} = (N_f, m_f, T, \mu_B), \quad \mathbf{v}_0 = (N_f, m_f, 0, 0). \quad (41)$$

In Eq. (40), $\Pi_{A; \mu\nu}$ is the vacuum polarization of the gluon that comprises all quantum, thermal, and density fluctuations in terms of the diagrams in the DSE. In a further step we split the diagrams in the thermal and density difference DSE into the gluonic part $\Delta\Pi_A^{\text{gl}}(k)$ whose classical three- or four-gluon vertex comes from the Yang-Mills sector, and the quark part $\Delta\Pi_A^{\text{qu}}(k)$ that is proportional to the classical quark-gluon vertex. The latter part is one-loop exact while the former one also contains two-loop diagrams.

$$\Delta\Pi_{A; \mu\nu}^{\mathbf{v}, \mathbf{v}_0}(k) = \Delta\Pi_{A; \mu\nu}^{\text{gl}; \mathbf{v}, \mathbf{v}_0}(k) + \Delta\Pi_{A; \mu\nu}^{\text{qu}; \mathbf{v}, \mathbf{v}_0}(k). \quad (42)$$

The quark loop contribution $\Delta\Pi_A^{\text{qu}}$ in Eq. (42) reads

$$\Delta\Pi_{A; \mu\nu}^{\text{qu}; \mathbf{v}, \mathbf{v}_0}(k) = \sum_f \left[\Pi_{A; \mu\nu}^{f; \mathbf{v}}(k) - \Pi_{A; \mu\nu}^{f; \mathbf{v}_0}(k) \right], \quad (43)$$

with

$$\Pi_{A; \mu\nu}^{f; \mathbf{v}}(k) = -\frac{1}{2} Z_{1F}^f g^2 \sum_q \text{tr} [\gamma_\mu S^f(\tilde{p}) \Gamma_\nu^f(k; \tilde{p}, \tilde{q}) S^f(\tilde{q})], \quad (44)$$

for each flavor. The trace in Eq. (44) sums over Dirac indices and gauge group indices in the fundamental

representation. The contribution is flavor diagonal as already assumed in the quark gap equation.

The pure gauge theory part can be evaluated analogously. While the difference does not require renormalization, the numerical implementation of this property requires some care and for this purpose a numerically stable scheme has been set up and successfully used in [12,22]. In the present work we resort to a further simplifying approximation suggested in [10,42] and expand the gauge loop contribution in Eq. (42) about the lattice data of the Yang-Mills (YM) gluon propagator. We obtain

$$\Delta\Pi_{A;\mu\nu}^{\mathbf{g}^1;\mathbf{v},\mathbf{v}_0}(k) = [D_{T;\mu\nu}^{\text{YM}}(k)]^{-1} - [D_{T=0;\mu\nu}^{\text{YM}}(k)]^{-1}, \quad (45)$$

where we have used that YM theory is only sensitive to the temperature and not the rest of the parameters in \mathbf{v} and \mathbf{v}_0 . The systematic error of this approximation for physical quark masses has been evaluated in detail in [11] and does not add significantly to the total systematic error for the T, μ_B regime considered here. In a forthcoming work this approximation is also resolved with the numerically stable scheme from [12,22].

Finally, we have to consider thermal and density splits in the vertices and especially in the quark-gluon vertex. The miniDSE approximation of the latter with two tensor structures has been introduced in Sec. II in the vacuum, see Eq. (26). At finite T, μ_B we have to take into account the thermal or density split of tensor structures as the heat bath or medium singles out a rest frame. To begin with, the classical tensor structure in Eq. (26) is split as

$$\gamma_\mu \Sigma_A(q, p) \rightarrow \gamma_\mu [\delta_{\mu 4} \Sigma_C(\tilde{q}, \tilde{p}) + (1 - \delta_{\mu 4}) \Sigma_A(\tilde{q}, \tilde{p})], \quad (46)$$

where \tilde{q}, \tilde{p} contain complex frequencies Eq. (37).

In the present work we employ the further simplification beyond the miniDSE scheme already discussed in the previous section on vacuum QCD: we only consider the second most important tensor structure $\mathcal{T}^{(4)}$ of the quark-gluon vertex, dropping the $\mathcal{T}^{(7)}$ contribution. Moreover, we use an RG-consistent split as in the vacuum. The vertex part with the second tensor structure $\mathcal{T}^{(4)}$ in Eq. (26) is split as follows:

$$\begin{aligned} &\mathcal{T}_\mu^{(4)}(q, p) \lambda^{(4)}(q, p) \\ &\rightarrow [\mathcal{T}^{(4)}]^\nu(q, p) \left[\Pi_{\mu\nu}^E(k) \lambda_E^{(4)}(q, p) + \Pi_{\mu\nu}^M(k) \lambda_M^{(4)}(q, p) \right], \end{aligned} \quad (47)$$

with the miniDSE approximation for the electric and magnetic dressing functions

$$\lambda_{E,M}^{(4)}(k; \tilde{q}, \tilde{p}) = g_s Z_{E,M}^{-1/2}(k^2) \Delta_B(\tilde{q}, \tilde{p}). \quad (48)$$

This concludes the discussion of the simplified version of the miniDSE scheme used in the present work: We have

reduced the task of solving the gap equations and vertex DSEs to that of solving the gap equations, where each approximation step has been benchmarked and controlled by functional results obtained within more sophisticated approximations as well as lattice results. We proceed by solving this set of difference DSEs for the quark and gluon dressings with the coupled quark and gluon DSEs [Eqs. (1) and (40)].

III. QCD PHASE STRUCTURE

We now present results for QCD phase structure, which are confronted with that obtained with lattice simulations and functional approaches at vanishing density and functional approaches at finite density. The latter results offer a quantitative benchmark up to densities $\mu_B/T \lesssim 4$. The calculation is performed in the isospin-symmetric approximation and with a vanishing strange quark chemical potential, $(\mu_u, \mu_d, \mu_s) = (1/3\mu_B, 1/3\mu_B, 0)$, which give the net-baryon number density $n_B = 2/3n_{u,d}$ and the vanishing strange quark density $n_s = 0$. This matches the scenario of heavy-ion collision with a vanishing net strangeness.

We define the pseudocritical temperature of the chiral phase transition $T_c(\mu_B)$ as the peak temperature of the thermal susceptibility of the reduced condensate $\Delta_{l,s}$ defined in Eq. (32),

$$\chi_T(T, \mu_B) = -\partial_T \left(\frac{\Delta_{l,s}(T, \mu_B)}{\Delta_{l,s}(0, 0)} \right). \quad (49)$$

Numerical results of χ_T at several chemical potentials are shown in Fig. 5. At zero μ_B , we obtain $T_c(0) = 156.5$ MeV in agreement with results from lattice QCD [16–18] and functional approaches [10–12,22,23].

A further benchmark result is provided with the curvature coefficients of the pseudocritical temperature at $\mu_B = 0$. Its Taylor at $\mu_B = 0$ is given by

$$\frac{T_c(\mu_B)}{T_c(0)} = 1 - \kappa_2 \left(\frac{\mu_B}{T_c(0)} \right)^2 - \kappa_4 \left(\frac{\mu_B}{T_c(0)} \right)^4 + \dots, \quad (50)$$

and the present simplified version of the miniDSE scheme yields

$$\kappa_2 = 0.0169(6). \quad (51)$$

This result is slightly larger but compatible with lattice QCD [16,17,43] and fRG/fRG-DSE [11,12,22] predictions with $\kappa_2 \approx 0.015$ [0.0142(2) in [11], 0.0147(5) in [12]]. On the other hand, we found $\kappa_4 \approx 5 \times 10^{-4}$ which is also larger but of the same magnitude as the functional results $\kappa_4 \approx 3 \times 10^{-4}$ in quantitative approximations [12].

These slight deviations grow larger at finite chemical potential. In Fig. 6 we depict the obtained phase transition line in Fig. 6 in comparison to other functional and lattice

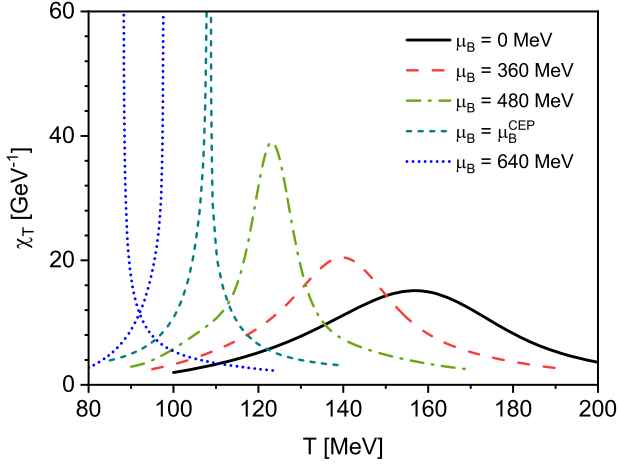


FIG. 5. Temperature dependence of the susceptibility χ_T at several quark chemical potentials, including $\mu_B^{\text{CEP}} = 567$ MeV. For the case of $\mu_B = 640$ MeV, the first order phase transition occurs and the χ_T for both Nambu and Wigner solutions are shown.

studies. Our result agrees well with the previous functional QCD results within more sophisticated truncations until $\mu_B \approx 400$ MeV or $\mu_B/T \approx 3$. For $\mu_B/T \gtrsim 3$ the deviations become sizable, which also manifests itself in the location of the critical end point (CEP) with

$$(T^{\text{CEP}}, \mu_B^{\text{CEP}}) = (108.5, 567) \text{ MeV}. \quad (52)$$

This location has to be contrasted with the quantitative estimate

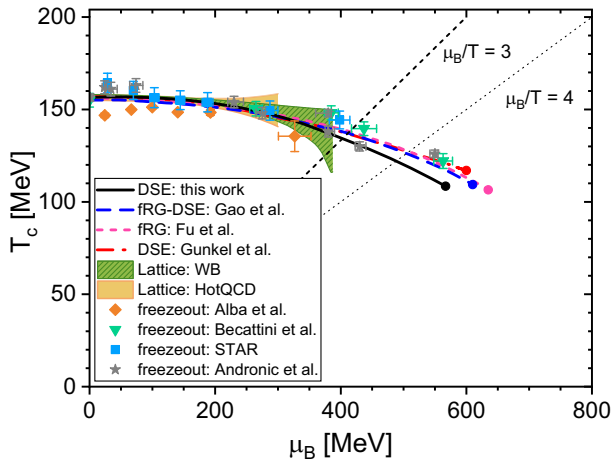


FIG. 6. Phase diagram obtained here within the simplified miniDSE scheme, compared to other functional QCD studies [11,22,23], lattice QCD extrapolation [16,17], and the extracted freeze-out data from different groups [44–47]. The present approximation to the minimal DSE scheme is reliable up to $\mu_B/T \lesssim 3$, which is marked by the black dashed line. We also display the reliability of the full quantitative computations [11,12], the dotted line with $\mu_B/T \lesssim 4$.

$$(T^{\text{CEP}}, \mu_B^{\text{CEP}}) \approx (100\text{--}110, 600\text{--}650) \text{ MeV}. \quad (53)$$

from the results in [11,12,22]. Considering the small error of the curvature obtained in Eq. (53), the phase transition temperature is well constrained. Therefore, the parameter space singles out a line instead of an area.

In short, Eq. (52) shows a $\sim 10\%$ deviation with respect to the estimate Eq. (53) and this deviation provides a systematic error estimate for the simplified miniDSE scheme used in the present work. In summary, this analysis entails that the simplified miniDSE scheme, provides semiquantitative results for a large range of chemical potentials. Hence, we can use it for the computation of thermodynamic quantities which are directly related to the measurements.

We close this section with a brief discussion of the twofold origin of the deviations, which are responsible for a successive loss of fully quantitative reliability of the present results for $\mu_B/T \gtrsim 3$. To begin with, we already know from the comparison of the phase structure computation in [22], that the use of full vacuum dressings for the quark-gluon vertex corrects the curvature coefficient κ . Moreover, the deviation at larger chemical potential is also caused by the use of Δ_B , Eq. (29), in the dressing $\lambda^{(4)}$, Eq. (30): in comparison to the dressing computed in [12], Δ_B carries a singular momentum dependence. This can be compensated for with the introduction of higher order corrections from the scattering kernel together with the imaginary part of the propagator induced by the chemical potential. An upgrade of the present simplified miniDSE scheme based on two-point dressings is work in progress and we hope to report on the respective results soon.

Another interesting aspect is the negligible contribution of the thermal chemical potential splits. For example, we find that the difference of chiral crossover temperature for the $O(4)$ -symmetric vertex without split and the vertex with thermal split is less than 1 MeV, and the curvature is barely changed. This result is also corroborated within a DSE computation with full vertices, [48] as well as many fRG tests, see, e.g., [14]. In conclusion, the split affects mainly the quark and gluon propagators, and the $O(4)$ -symmetric approximation for the quark-gluon vertex gives agreeing results for $\mu_B/T \gtrsim 3$ as discussed above. Note, however, that the explicit results here are obtained within the thermal split.

IV. EQUATION OF STATE OF QCD

The miniDSE scheme allows for a numerically cheap complete scan of the EOS and other observables in the phase diagram of QCD. In the present work we also employ the further simplification beyond the miniDSE scheme described in Secs. II C and II D and tested in Sec. III.

In Sec. IV A we present results for the quark number density and the pressure. These results are accompanied by further derived observables, the entropy and energy

densities as well as the ratio of pressure to energy density. In Sec. IV B these results are used to compute the isentropic trajectories, and the speed of sound in Sec. IV C. Finally, we discuss extrapolations in the phase structure in Sec. IV D.

A. Thermodynamic observables

The quark number densities n_q^f are directly obtained from the quark propagators,

$$n_q^f(T, \mu_B) \simeq -N_c Z_2^f T \sum_n \int \frac{d^3 p}{(2\pi)^3} \text{tr}_D [\gamma_4 S^f(p)], \quad (54)$$

where we use $\mu_B = 3\mu_l$ with $\mu_u = \mu_d = \mu_l$ and $\mu_s = 0$. In the present work we simply use the momentum-dependent propagators in the $T - \mu_B$ plane on the right-hand side of Eq. (54) and leave a more detailed analysis to future work.

First, it is well known that Eq. (54) has to be evaluated in the nonvanishing background $\langle A_0 \rangle$ that solves the equations of motion, see [49,50]. This is tantamount to implementing the nontrivial expectation value of the Polyakov loop away from unity. Only with such a background the change from quark-gluon degrees of freedom to hadronic ones is described accurately. This is well illustrated with the kurtosis whose asymptotic temperature values is 1/9 in the quark-gluon phase for large temperatures and unity in the hadronic phase for vanishing temperature, capturing the change of the degrees of freedom from asymptotically free quarks to weakly interacting baryons. Without the A_0 background, the degrees of freedom in the low temperature phase resemble the quarks and the kurtosis is far smaller than unity; for a detailed discussion see [51]. In short, with $\langle A_0 \rangle = 0$ the qualitative behavior around the crossover line with its change of the dynamical degrees of freedom is captured, for the quantitative or even semiquantitative behavior the A_0 background is required. Respective results and formal developments in functional approaches can be found in [11,52–55,55].

Second, the density Eq. (54) requires renormalization and is subject to a nontrivial normalization, reflecting its UV degree of divergence. This intricacy worsens at large temperatures but can be resolved by representing the density in terms of a (multiple) chemical potential integration of density fluctuations with a lower or absent UV degree of divergence, e.g., the kurtosis. Indeed, the thermodynamic relation between pressure and quark number density discussed below is precisely of this type as the quark number density has a lower UV degree of divergence.

Both issues will be addressed in a forthcoming work and we proceed with the present qualitative approximation. The EOS follows from n_q^f in the (T, μ_B) plane with the thermodynamic relation between the pressure and quark number densities,

$$P(T, \mu_B) = P(T, 0) + \frac{1}{3} \int_0^{\mu_B} d\mu n_l(T, \mu), \quad (55)$$

where $n_l = n_q^u + n_q^d$. The standard thermodynamic relation Eq. (55) is of the same structural form as our difference DSE: The integral in Eq. (55) is simply $\Delta P(T, \mu_B) = P(T, \mu) - P(T, 0)$ and follows from the quark propagators. In turn, the pressure at vanishing chemical potential can be determined from the QCD trace anomaly $I(T)$,

$$I(T) = (\epsilon - 3P)/T^4, \quad (56)$$

with

$$P(T, \mathbf{0})/T^4 = \int_0^T dT' (I(T')/T'). \quad (57)$$

For $I(T)$ we use 2 + 1 flavor QCD lattice data [56]. Moreover, the integral over the quark number density expresses the density part of the pressure in terms of a less-divergent operator which stabilizes the numerical computation and lowers the systematic error.

In summary, with the lattice input for the trace anomaly at $\mu_B = 0$ and the relations Eq. (54)(55), we can compute the QCD pressure $P(T, \mu_B)$, the energy density ϵ , and the entropy density s and in the $T - \mu_B$ plane,

$$\begin{aligned} \epsilon(T, \mu_B) &= Ts(T, \mu_B) + \mu_B n_B(T, \mu_B) - P(T, \mu_B), \\ s(T, \mu_B) &= \partial P(T, \mu_B) / \partial T. \end{aligned} \quad (58)$$

The respective numerical results for the pressure P/P_{SB} and the light quark number density $n_{u,d}/T^3$ are shown in Fig. 7 and provide us with the EOS. Further thermodynamic observables, namely the entropy density s/s_{SB} , the energy density $\epsilon/\epsilon_{\text{SB}}$, and pressure to energy density ratio P/ϵ are shown in Fig. 8. We have normalized the pressure and energy density with the free Stefan-Boltzmann counterparts in three flavor QCD at zero chemical potential,

$$P_{\text{SB}} = \frac{19}{36} \pi^2 T^4, \quad s_{\text{SB}} = \frac{19}{9} \pi^2 T^3, \quad \epsilon_{\text{SB}} = \frac{19}{12} \pi^2 T^4. \quad (59)$$

In the vicinity of the CEP, the entropy s and the energy density ϵ experience rapid changes close to the chiral crossover line $T_c(\mu_B)$. This rapid change indicates the increasingly rapid change of the degrees of freedom from hadrons to quarks in the vicinity of crossover. Moreover, the successively sharper and deeper minimum of P/ϵ is related to the peak of the trace anomaly in Eq. (57) as well as the minimum of the speed of sound, and leaves a strong imprint on the EOS. The latter allows us to estimate the location of the CEP even relatively far away from it.

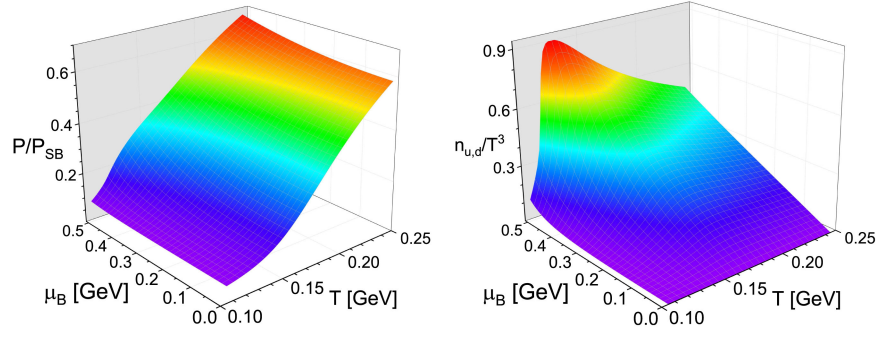


FIG. 7. Light quark number density $n_{u,d}$ and QCD pressure P , normalized by the Boltzmann limit Eq. (59), at finite temperature T and baryon chemical potential μ_B .

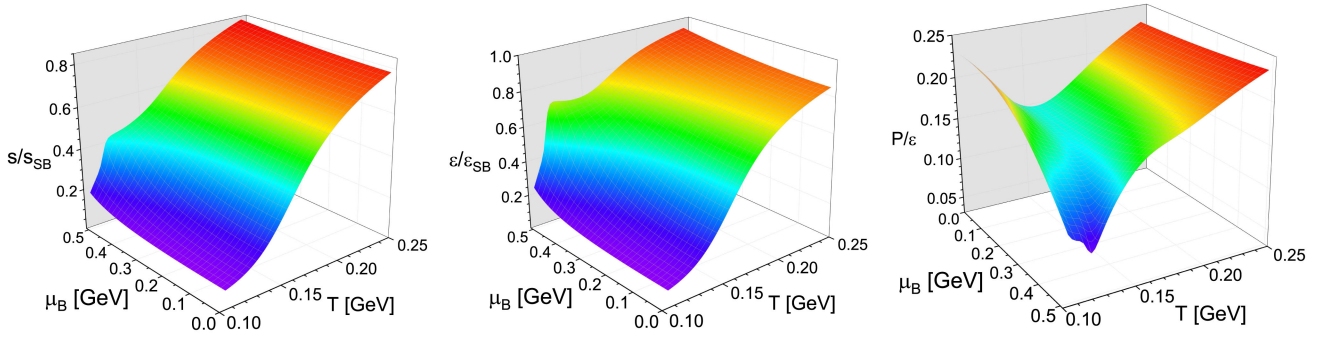


FIG. 8. Calculated entropy density s , energy density ϵ , which are scaled by their Boltzmann limits Eq. (59), and the ratio of pressure to energy density P/ϵ .

B. Isentropic trajectories

We have also investigated the isentropic trajectories, i.e., the trajectories satisfying $s/n_B = \text{const}$ in the (T, μ_B) plane, which are related to the cooling of the hot quark gluon plasma matter produced in heavy-ion collision experiments. The isentropic trajectories calculated from our EOS at these s/n_B values are shown in Fig. 9, together with the chiral phase transition line and the CEP. We also compare the obtained phase diagram and the trajectories to the freeze-out data, which are marked with the same labels as in Fig. 6. In the vicinity of the phase transition line, our calculated trajectories are in good agreement with those obtained from the state-of-the-art equation of state named NEoS in [57,58]. Especially, our trajectories for $s/n_B = 420, 144, 51,$ and 30 whose values are chosen in the previous studies for the corresponding collision energies in heavy ion collision experiments, also precisely meet with the freeze-out points at $\sqrt{s_{NN}} = 200, 62.4, 19.6,$ and 11.5 GeV, respectively.

At high temperatures, our results deviate from the trajectories from lattice QCD simulation and we can trace this back to the normalization intricacy of the quark number density discussed below Eq. (54). In turn, below the crossover line the background $\langle A_0 \rangle$ [10,11,49,50,59] has not been incorporated in the present computations of the

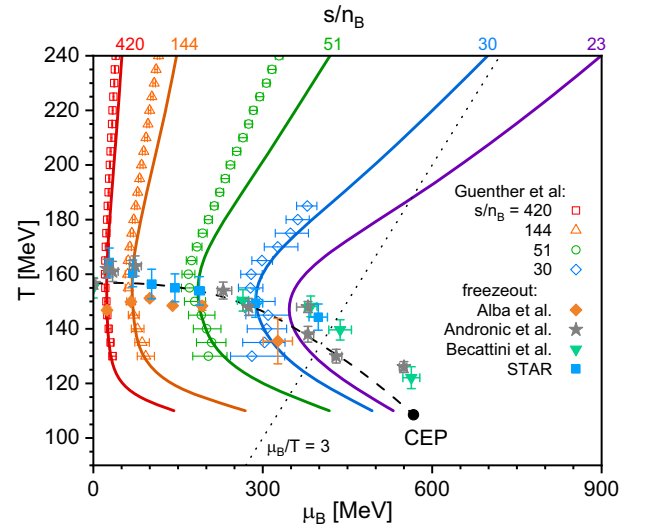


FIG. 9. Isentropic trajectories for several values of s/n_B together with QCD phase diagram; the black-dashed curve stands for the chiral crossover phase transition line. The trajectories are consistent with the lattice QCD calculation as shown with the open points [57]. The filled points mark the freeze-out points from Refs. [44–47].

density or other thermodynamic quantities and has a significant impact. A full quantitative computation is beyond the scope of the present paper and will be presented elsewhere.

In addition to the s/n_B values obtained from the extrapolation of lattice data at vanishing density, we also have investigated a smaller value with $s/n_B = 23$ with the present EOS. By comparing the result with the STAR freeze-out points [46], we estimate that $s/n_B = 23$ corresponds to $\sqrt{s_{\text{NN}}} \gtrsim 7.7$ GeV. This estimate should be taken with a grain of salt as the curve is located at the border of (and beyond) the quantitative reliability regime of the present simplified miniDSE scheme, and we have neither tackled the A_0 background nor the normalization issue. With this caveat we note that this trajectory still does not cross the CEP, and it may require a smaller collision energy for approaching it.

C. Speed of sound

Finally, we report results for the speed of sound c_s in the simplified miniDSE scheme. We have computed c_s^2 in the vicinity of the phase transition line. In order to investigate the experimental scenario of adiabatic cooling, the speed of sound is evaluated along the isentropic trajectories, using the following formula [60]:

$$c_s^2 = \frac{n_B^2 \partial_T^2 P - 2s n_B \partial_T \partial_{\mu_B} P + s^2 \partial_{\mu_B}^2 P}{(\epsilon + P) [\partial_T^2 P \partial_{\mu_B}^2 P - (\partial_T \partial_{\mu_B} P)^2]}. \quad (60)$$

The temperature T is chosen as the control parameter for each trajectory, and the results are shown in Fig. 10. The minimum of $c_s^2(T)$ agrees with the chiral phase transition point for each trajectory. The value of the speed of sound at the minimum does not change too much in the current energy range, as $c_s^2 \sim 0.13$, but the minimum becomes sharper as s/n_B decreases.

The speed of sound is computed from the second and fourth order T, μ_B derivatives of QCD pressure, see Eq. (60), including for example the mixed μ_B, T derivative, the thermal susceptibility of the baryon number, as well as its derivative. Its minimum may be regarded as a criterion for the crossover temperature of the confinement-deconfinement phase transition. This crossover can also be measured more directly in terms of fluctuations of baryonic charges, see [55] for recent functional results. We observe that the crossover temperature is a bit lower as the chiral crossover temperature defined by the peak of the thermal susceptibility of the chiral condensate, Eq. (49), even though this difference does not exceed the respective error bars and the widths of these transitions. With increasing μ_B the transition regime gets sharper as the region around the minimum of c_s^2 is getting steeper. Hence, both the chiral and confinement-deconfinement phase transitions get steeper towards the critical end point as expected.

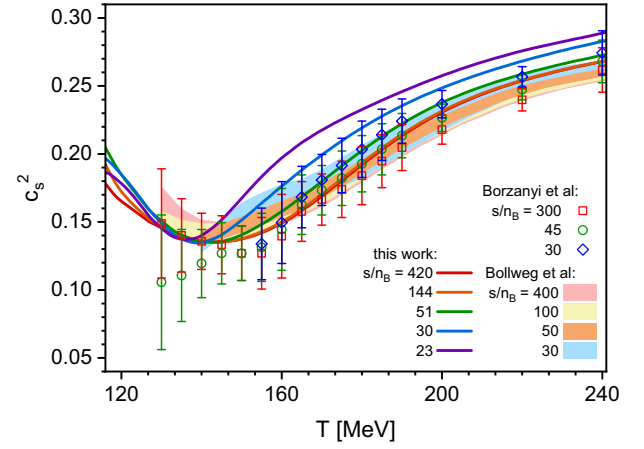


FIG. 10. Speed of sound squared c_s^2 in isentropic evolution as a function of temperature T along the trajectories in Fig. 9, labeled with their s/n_B values. Results from the lattice calculation Refs. [19,58] are also attached for comparison.

D. Extrapolations in the phase structure

Note that we do not observe critical scaling; for a more detailed analysis see [55]. However, it is precisely the smallness of the critical regime, observed by now for both the O(4)-scaling regime in the chiral limit, [61–63] and around the critical end point [64], that allows for a precision estimate of the location of the latter: the extrapolation of *suitable* nonuniversal observables towards higher chemical potentials provides a quantitative estimate of the location of the CEP, if the data are sufficiently accurate. Such an endeavor requires a theoretical search for and quantitative computation of optimal observables in the phase structure together with their extraction from high precision experimental data. A respective program has been advocated and started in [54,55] with the theoretical computation and the comparison to experimental data of fluctuations of observed charges.

In the present work, we contribute to this program by comparing the estimates of the location of the critical end point from several thermodynamic functions with the computed location in the present simplified miniDSE scheme, see Fig. 11. To that end we consider the thermal width ΔT for both thermal susceptibilities χ_T and $\partial n_B / \partial T$, which is defined as the width of the 90% value of the peak heights of the respective susceptibility. In case of P/ϵ the width ΔT is defined as the width of 110% value of the minimum. These thermal widths monotonously decrease for larger chemical potential and vanish at the CEP. Hence, an extrapolation of the widths towards zero provides us with an estimate of the location of the CEP. A fully conclusive analysis will be presented elsewhere and will answer the question about the required precision and wealth of the experimental data for such a quantitative estimate in dependence of the distance to the CEP in terms of chemical potential or collision energy \sqrt{s} .

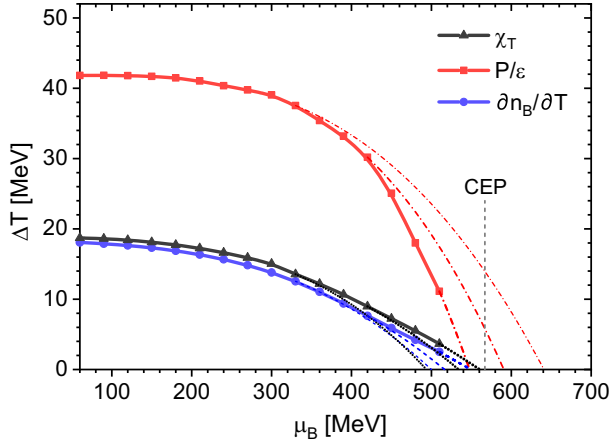


FIG. 11. Estimates for the location of the critical end point from the extrapolation of the thermal width ΔT , using the thermal susceptibility of the chiral condensate $\chi_T \propto \partial_T \partial_m P$, the thermal susceptibility of the baryon number density $\partial n_B / \partial T = \partial_T \partial_{\mu_B} P$, and that of the ratio of pressure to the energy density P/ϵ . The width ΔT is calculated as the width of the 90% peak height for χ_T and $\partial n_B / \partial T$, or the 110% value of the minimum for P/ϵ . The extrapolation of ΔT is performed using the data within $\mu_B \leq 330, 420,$ and 510 MeV, respectively, and the extrapolated CEP position is at $\Delta T = 0$. The actual CEP position of $\mu_B = 567$ MeV is also displayed by the gray-dashed line.

Here we proceed by simply elucidating this task with a limited amount of data points, see Fig. 11. We perform cubic polynomial fits for the ΔT data within several μ_B regions and then extrapolate towards larger μ_B . For current ΔT data, adding higher order polynomial terms only changes the extrapolated CEP position for about 5% and thus a cubic fit is sufficient for convergence. We find that with successively larger μ_B included into the fit regime, the estimates for the location of the CEP get closer to its actual location. However, even with the present sparse data one does not have to zoom into the neighborhood of the CEP. Moreover, the comparison shows that the chiral condensate or rather its susceptibility is better suited for such an extrapolation. In summary, it is very suggestive that a global combination of experimental precision data is best suited for such a task. This asked for the latter, which can be obtained in a combination of STAR data and in particular future high precision CBM data, based on its orders of magnitude larger luminosity.

V. SUMMARY

In the present work we have computed thermodynamic quantities such as the chiral phase structure, the QCD equation of state (EOS), the isentropic trajectories, and the speed of sound within first principles functional QCD. At low densities, the results are benchmarked with lattice results, while at larger densities the current approach offers qualitative predictions. The EOS was obtained from integrating the quark number density from vanishing to finite chemical potential, while using lattice results for the trace

anomaly at zero chemical potential as an input. Apart from the above mentioned observables we have also computed the pressure, entropy density, and energy density in a wide range of temperature and chemical potential. In particular, we also discussed the implications of our results for the adiabatic speed of sound on the search for novel phases and the location of critical end point in the strong interaction matter produced in the collider experiments.

Our thermodynamic results are obtained within a minimal computational scheme for functional approaches, developed in the present work for quantitative and semiquantitative computations, see Secs. II and IID. This scheme is also based on previous developments in [11,12,22] both in the DSE approach as well as in the fRG approach. Here we have applied its DSE version, the miniDSE scheme, to computations of the quark propagator at finite temperature and density. Additional truncations reduced the regime of quantitative reliability to the regime $\mu_B/T \lesssim 3$, where the current results for the phase structure agree very well with that in state-of-the-art quantitative truncations [11,12,23]. Still, also the results in the regime $\mu_B/T \gtrsim 3$ provide semiquantitative and qualitative estimates. For example, the current estimate of the location of the critical end point only differs by approximately 10% by that given in the quantitative studies. This leads us to the suggestion to finally determine its location within a combination of theoretical constraints and predictions for both, the phase structure as well as experimental observables, and respective experimental precision measurements.

While the current application has been tuned to minimal computational costs and further truncations have been done, aiming at the computation in terms of two-point functions alone, the fully quantitative miniDSE scheme is set up as well. Moreover, the miniDSE scheme can also be readily applied to the low temperature and finite chemical potential regime, i.e., cold dense quark matter and the equation of state of neutron stars. Furthermore, it provides a simple and quantitative access for the exploration of the QCD phase structure in the (T, m_l, m_s) space, the Columbia plot, which is work under completion.

We hope to report soon on the respective results in the Columbia plot and for cold dense matter, and in particular on a precision prediction for experimentally accessible observables in the regime $2 \text{ GeV} \lesssim \sqrt{s} \lesssim 15 \text{ GeV}$. This regime includes the location of the critical end point or more generally the onset regime of new phases: Theoretical predictions accompanied with an analysis of the μ_B or \sqrt{s} dependence, and a combination of STAR data and future high precision CBM data in this regime should allow us to finally pin down the location of the CEP or the onset regime of new phases as well as its physics.

ACKNOWLEDGMENTS

We thank G. Eichmann, C. S. Fischer, W.-j. Fu, M. Q. Huber, J. Papavassiliou, F. Rennecke, B.-J. Schaefer, N. Wink,

and Hui-Wen Zheng for discussions. This work is done within the fQCD collaboration [65], and we thank the members of the collaboration for discussions and collaboration on related subjects. This work is funded by the Deutsche Forschungsgemeinschaft (DFG, German Research Foundation) under Germany's Excellence Strategy EXC 2181/1-390900948 (the Heidelberg STRUCTURES Excellence Cluster) and the Collaborative Research Centre SFB 1225-273811115 (ISOQUANT). Y.L. and Y.X.L. are supported by the National Science Foundation of China under Grants No. 12175007 and No. 12247107. F.G. is supported by the National Science Foundation of China under Grant No. 12305134.

APPENDIX A: PARAMETRIZED FORMULA OF THE VACUUM GLUON AND GHOST PROPAGATORS

In our computations we use the parametrization in [24] of the $2+1$ -flavor gluon propagator in the vacuum equation (22), which combines the data from quantitative functional QCD and from lattice QCD [11,12,22,66,67],

$$G_A(k^2) = \frac{\frac{a^2+k^2}{b^2+k^2}}{M_G^2(k^2) + k^2[1 + c \log(d^2k^2 + e^2M_G^2(k^2))]^\gamma},$$

$$M_G^2(k^2) = \frac{f^4}{g^2 + k^2}, \quad \gamma = \frac{13 - \frac{4}{3}N_f}{22 - \frac{4}{3}N_f}, \quad (\text{A1})$$

where γ is the anomalous dimension of the one-loop gluon propagator and

$$a = 1 \text{ GeV}, \quad b = 0.735 \text{ GeV}, \quad c = 0.12,$$

$$d = 0.0257 \text{ GeV}^{-1}, \quad e = 0.081 \text{ GeV}^{-1},$$

$$f = 0.65 \text{ GeV}, \quad g = 0.87 \text{ GeV}. \quad (\text{A2})$$

For the ghost dressing function $F(k^2)$ in Eq. (27), the vacuum fRG data in two-flavor QCD is taken from Ref. [31], which is parametrized as

$$F(k^2) = \frac{\frac{a_1+b_1\sqrt{k^2+k^2}}{c_1+d_1\sqrt{k^2+k^2}}}{[1 + e_1 \ln(f_1^2k^2 + g_1^2M_G^2(k^2))]^\delta}, \quad (\text{A3})$$

where M_G is the same as in Eq. (A1), with $\delta = 0.27$ the anomalous dimension, and

$$a_1 = 0.152 \text{ GeV}^2, \quad b_1 = 0.697 \text{ GeV},$$

$$c_1 = 0.0055 \text{ GeV}^2, \quad d_1 = 0.016 \text{ GeV}, \quad e_1 = 0.045,$$

$$f_1 = 0.025 \text{ GeV}^{-1}, \quad g_1 = 0.0237 \text{ GeV}^{-1}. \quad (\text{A4})$$

Equations Eq. (A1) and (A3) fit the functional and lattice data well in the regime $p \in [0, 40]$ GeV, and hence cover the momenta relevant for the present computations.

APPENDIX B: ERROR ESTIMATE OF THE KINEMATIC SINGULARITY

As a part of the evaluation on the kinematic singularity effect in Eq. (30), we first argue that the kinematic singularity can be avoided by the following upgrade of the present procedure: Instead of using Eq. (21) and its finite temperature and chemical potential analogs for the definition of the gluon wave function, one can use a parametrization for the scalar propagator part $G_A(k)$ in Eq. (21), which takes into account the mass gap of QCD explicitly. In the vacuum this reads

$$G_A(k) = \frac{1}{Z_{A,\text{scr}}(k)} \frac{1}{k^2 + m_{\text{scr}}^2}, \quad (\text{B1})$$

where m_{scr}^2 is the spatial screening mass. This mass is defined via the exponential decay of the large distance limit of the spatial Fourier transform of the gluon propagator,

$$\tilde{G}_A(k_0, r) = \int \frac{d^3k}{(2\pi)^3} G_A(k_0, \mathbf{k}) e^{i\mathbf{k}\mathbf{x}}, \quad (\text{B2})$$

with the spatial momentum \mathbf{k} and the spatial position or distance \mathbf{x} and $r = \|\mathbf{x}\|$. The large distance limit $r \rightarrow \infty$ can be parametrized with

$$\lim_{r \rightarrow \infty} \tilde{G}_A(k_0 = 0, r) \rightarrow R(r) e^{-m_{\text{scr}} r}, \quad (\text{B3})$$

where $R(r)$ is a polynomial or at most a rational function of r . The spatial screening mass m_{scr}^2 is the inverse screening length and is defined as the strength of the exponential decay. A similar definition holds true for the temporal screening mass, which is obtained from the asymptotic time dependence of the Schwinger function.

In the vacuum these two masses agree due to Lorentz invariance and we get from the functional and lattice $2+1$ gluon data in [11,12,22,25,67],

$$m_{\text{scr}} \approx 850 \text{ MeV}. \quad (\text{B4})$$

The overall error of Eq. (B4) and the respective ones for $N_f = 2$ flavor QCD and Yang-Mills theory is about 20 MeV which can be reduced significantly if producing dedicated data for the task of determining the screening mass. Equation (B4) can be considered as a physics definition of the gluon mass gap, and can be compared with $m_{\text{scr}} \approx 830$ MeV for the two-flavor data from [31] that underlie the $2+1$ flavor computations in [11,12,22] and $m_{\text{scr}} \approx 760$ MeV in Yang-Mills theory from the gluon data in [68], compatible with the $T \rightarrow 0$ extrapolation of the finite temperature screening mass computed in [69]. The physical nature of this definition is corroborated by the quantitative agreement of the screening mass with the Debye screening mass in thermal perturbation theory for

temperatures $T \gtrsim 2T_c$, where T_c is the critical temperature of the confinement-deconfinement phase transition.

The spatial and temporal screening masses differ at finite temperature and chemical potential, and a more quantitative vertex construction at finite temperature and chemical potential takes into account both screening masses. For a respective discussion and computation in finite temperature Yang-Mills theory, see [69], and the notation in Eq. (B1) is close to that used there and in further fRG works such as [11] and the DSE works [12,22,24,62].

We emphasize that the spatial and temporal screening masses reflect the physical gluon mass gap in QCD even in the present gauge-fixed settings and constitute a relevant physics input in phenomenological considerations in the phase structure of QCD. This is already evident for its importance for the confinement-deconfinement phase transition in Yang-Mills theory, see [69]. Importantly, with the substitution

$$Z^{1/2}(k) \rightarrow \frac{1}{Z_{A,\text{scr}}^{1/2}(k)}, \quad (\text{B5})$$

in Eq. (30) as well as other dressings, kinematic singularities are avoided and the respective dressings reflect the decoupling of the dynamics below the (gluon) mass gap of QCD. This as well as their phenomenological importance will be considered elsewhere.

For the present purposes we find that the simplified vertex construction Eq. (30) serves well and the kinematic singularity has no impact on the physics considered here. We proceed with the systematic error estimate with a comparison to results with the full vertex. First, we note that the negligible impact of this kinematic singularity has been discussed in detail in [22], based on the explicit vacuum results in [28–31]. Importantly, this analysis has also been extended to finite T and μ_B in [12]. Below we briefly discuss these different checks.

In [22], it has been shown that Eq. (30) describes the $\mathcal{T}^{(4)}$ structure of the full vertex in the vacuum very well down to momenta $k \approx 1$ GeV, using also vertex data from [31]. This has later been corroborated with vertex data from the quantitative DSE vacuum computation in [24]. In turn, for $k \lesssim 500$ MeV, the vertex Eq. (30) shows a kinematic singularity which is not present in the full vertex that monotonously rises and approaches a constant for $k = 0$.

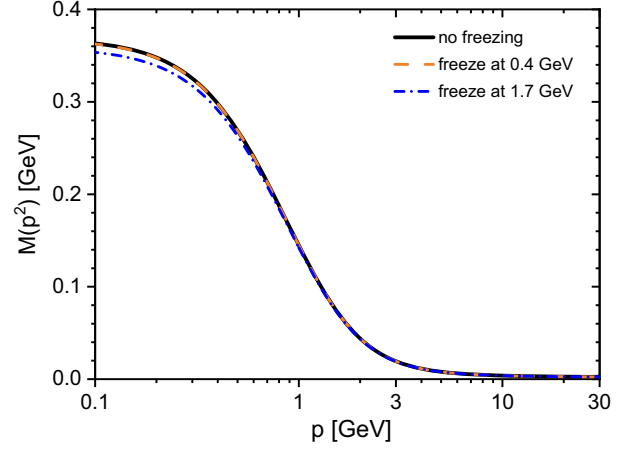


FIG. 12. A comparison of the calculated quark mass function $M(p^2)$ in the vacuum: with no freezing, and with a freezing $Z(k)$ for $k \in [0, 1/2m_{\text{scr}}] = [0, 0.4]$ GeV and for $k \in [0, 2m_{\text{scr}}] = [0, 1.7]$ GeV.

The kinematic singularity in Eq. (30) is in a regime which is suppressed by the mass gap of QCD, and hence it has no impact. This has been checked and confirmed in several ways: Its reliability for computations in the phase structure has been benchmarked with the good agreement of the results with that from [11] up to baryon chemical potentials $\mu_B \lesssim 600$ MeV, and this has been corroborated by the phase structure results with the direct computation of quark-gluon vertex DSEs in [12]. In the present work we check the irrelevance of the kinematic singularity by freezing $Z(k)$ in Eq. (30) for small momenta with a freezing scale in the regime

$$k_{\text{freeze}} \approx 0.4\text{--}1.7 \text{ GeV}, \quad (\text{B6})$$

which is roughly $1/2m_{\text{scr}} \lesssim k_{\text{freeze}} \lesssim 2m_{\text{scr}}$ with the $2 + 1$ flavor screening mass in Eq. (B4). This emulates the effect of Eq. (B5) as $Z_{A,\text{scr}}$ indeed freezes for small momenta. Moreover, it covers efficiently the difference to the full vertex: while the kinematic singularity leads to an enhancement of the vertex, the freezing leads to a lowering of the vertex in comparison to the full vertex. The results do not change by more than 3%, for example in the vacuum the freezing effect on the quark mass function is shown in Fig. 12. This is well within the systematic error estimate of our computation and, hence, supports our procedure.

-
- [1] S. P. Klevansky, *Rev. Mod. Phys.* **64**, 649 (1992).
 [2] M. Buballa, *Phys. Rep.* **407**, 205 (2005).
 [3] K. Fukushima and C. Sasaki, *Prog. Part. Nucl. Phys.* **72**, 99 (2013).

- [4] K. Fukushima and V. Skokov, *Prog. Part. Nucl. Phys.* **96**, 154 (2017).
 [5] S. J. Freedman, *Nuclear Physics: Exploring the Heart of Matter* (The National Academies Press, Washington, DC, 2013).

- [6] D. H. Rischke, *Prog. Part. Nucl. Phys.* **52**, 197 (2004).
- [7] M. Oertel, M. Hempel, T. Klähn, and S. Typel, *Rev. Mod. Phys.* **89**, 015007 (2017).
- [8] S.-x. Qin, L. Chang, H. Chen, Y.-x. Liu, and C. D. Roberts, *Phys. Rev. Lett.* **106**, 172301 (2011).
- [9] C. S. Fischer and J. Luecker, *Phys. Lett. B* **718**, 1036 (2013).
- [10] C. S. Fischer, J. Luecker, and C. A. Welzbacher, *Phys. Rev. D* **90**, 034022 (2014).
- [11] W.-j. Fu, J. M. Pawłowski, and F. Rennecke, *Phys. Rev. D* **101**, 054032 (2020).
- [12] F. Gao and J. M. Pawłowski, *Phys. Lett. B* **820**, 136584 (2021).
- [13] C. S. Fischer, *Prog. Part. Nucl. Phys.* **105**, 1 (2019).
- [14] N. Dupuis, L. Canet, A. Eichhorn, W. Metzner, J. M. Pawłowski, M. Tissier, and N. Wschebor, *Phys. Rep.* **910**, 1 (2021).
- [15] W.-j. Fu, *Commun. Theor. Phys.* **74**, 097304 (2022).
- [16] S. Borsanyi, Z. Fodor, J. N. Guenther, R. Kara, S. D. Katz, P. Parotto, A. Pasztor, C. Ratti, and K. K. Szabo, *Phys. Rev. Lett.* **125**, 052001 (2020).
- [17] A. Bazavov *et al.* (HotQCD Collaboration), *Phys. Lett. B* **795**, 15 (2019).
- [18] C. Bonati, M. D'Elia, F. Negro, F. Sanfilippo, and K. Zambello, *Phys. Rev. D* **98**, 054510 (2018).
- [19] S. Borsanyi, G. Endrodi, Z. Fodor, S. D. Katz, S. Krieg, C. Ratti, and K. K. Szabo, *J. High Energy Phys.* **08** (2012) 053.
- [20] A. Bazavov *et al.*, *Phys. Rev. D* **95**, 054504 (2017).
- [21] S. Borsányi, Z. Fodor, J. N. Guenther, R. Kara, S. D. Katz, P. Parotto, A. Pásztor, C. Ratti, and K. K. Szabó, *Phys. Rev. Lett.* **126**, 232001 (2021).
- [22] F. Gao and J. M. Pawłowski, *Phys. Rev. D* **102**, 034027 (2020).
- [23] P. J. Gunkel and C. S. Fischer, *Phys. Rev. D* **104**, 054022 (2021).
- [24] F. Gao, J. Papavassiliou, and J. M. Pawłowski, *Phys. Rev. D* **103**, 094013 (2021).
- [25] P. Boucaud, F. De Soto, K. Raya, J. Rodríguez-Quintero, and S. Zafeiropoulos, *Phys. Rev. D* **98**, 114515 (2018).
- [26] A. C. Aguilar, F. De Soto, M. N. Ferreira, J. Papavassiliou, J. Rodríguez-Quintero, and S. Zafeiropoulos, *Eur. Phys. J. C* **80**, 154 (2020).
- [27] L. Chang, Y.-X. Liu, and C. D. Roberts, *Phys. Rev. Lett.* **106**, 072001 (2011).
- [28] R. Williams, *Eur. Phys. J. A* **51**, 57 (2015).
- [29] M. Mitter, J. M. Pawłowski, and N. Strodthoff, *Phys. Rev. D* **91**, 054035 (2015).
- [30] R. Williams, C. S. Fischer, and W. Heupel, *Phys. Rev. D* **93**, 034026 (2016).
- [31] A. K. Cyrol, M. Mitter, J. M. Pawłowski, and N. Strodthoff, *Phys. Rev. D* **97**, 054006 (2018).
- [32] C. Tang, F. Gao, and Y.-X. Liu, *Phys. Rev. D* **100**, 056001 (2019).
- [33] L. Chang, Y.-B. Liu, K. Raya, J. Rodríguez-Quintero, and Y.-B. Yang, *Phys. Rev. D* **104**, 094509 (2021).
- [34] G. Eichmann, H. Sanchis-Alepuz, R. Williams, R. Alkofer, and C. S. Fischer, *Prog. Part. Nucl. Phys.* **91**, 1 (2016).
- [35] L. Chang and C. D. Roberts, *Phys. Rev. C* **85**, 052201 (2012).
- [36] S.-X. Qin, L. Chang, Y.-X. Liu, C. D. Roberts, and S. M. Schmidt, *Phys. Lett. B* **722**, 384 (2013).
- [37] F. Gao and Y.-x. Liu, *Phys. Rev. D* **94**, 076009 (2016).
- [38] O. Oliveira, A. Kizilersu, P. J. Silva, J.-I. Skullerud, A. Sternbeck, and A. G. Williams, *Acta Phys. Pol. B Proc. Suppl.* **9**, 363 (2016).
- [39] L.-f. Chen, Z. Bai, F. Gao, and Y.-x. Liu, *Phys. Rev. D* **104**, 094041 (2021).
- [40] R. Williams, C. S. Fischer, and M. R. Pennington, *Phys. Lett. B* **645**, 167 (2007).
- [41] S. Aoki *et al.* (Flavour Lattice Averaging Group Collaboration), *Eur. Phys. J. C* **80**, 113 (2020).
- [42] G. Eichmann, C. S. Fischer, and C. A. Welzbacher, *Phys. Rev. D* **93**, 034013 (2016).
- [43] P. Cea, L. Cosmai, and A. Papa, *Phys. Rev. D* **89**, 074512 (2014).
- [44] P. Alba, W. Alberico, R. Bellwied, M. Bluhm, V. Mantovani Sarti, M. Nahrgang, and C. Ratti, *Phys. Lett. B* **738**, 305 (2014).
- [45] F. Becattini, J. Steinheimer, R. Stock, and M. Bleicher, *Phys. Lett. B* **764**, 241 (2017).
- [46] L. Adamczyk *et al.* (STAR Collaboration), *Phys. Rev. C* **96**, 044904 (2017).
- [47] A. Andronic, P. Braun-Munzinger, K. Redlich, and J. Stachel, *Nature (London)* **561**, 321 (2018).
- [48] Y. Lu, F. Gao, J. M. Pawłowski, and C. Schneider (to be published).
- [49] J. Braun, H. Gies, and J. M. Pawłowski, *Phys. Lett. B* **684**, 262 (2010).
- [50] L. Fister and J. M. Pawłowski, *Phys. Rev. D* **88**, 045010 (2013).
- [51] W.-j. Fu and J. M. Pawłowski, *Phys. Rev. D* **92**, 116006 (2015).
- [52] W.-j. Fu and J. M. Pawłowski, *Phys. Rev. D* **93**, 091501 (2016).
- [53] W.-j. Fu, J. M. Pawłowski, F. Rennecke, and B.-J. Schaefer, *Phys. Rev. D* **94**, 116020 (2016).
- [54] W.-j. Fu, X. Luo, J. M. Pawłowski, F. Rennecke, R. Wen, and S. Yin, *Phys. Rev. D* **104**, 094047 (2021).
- [55] W.-j. Fu, X. Luo, J. M. Pawłowski, F. Rennecke, and S. Yin, *arXiv:2308.15508*.
- [56] S. Borsanyi, G. Endrodi, Z. Fodor, A. Jakovac, S. D. Katz, S. Krieg, C. Ratti, and K. K. Szabo, *J. High Energy Phys.* **11** (2010) 077.
- [57] J. N. Guenther, R. Bellwied, S. Borsanyi, Z. Fodor, S. D. Katz, A. Pasztor, C. Ratti, and K. K. Szabó, *Nucl. Phys.* **A967**, 720 (2017).
- [58] D. Bollweg, D. A. Clarke, J. Goswami, O. Kaczmarek, F. Karsch, S. Mukherjee, P. Petreczky, C. Schmidt, and S. Sharma (HotQCD Collaboration), *Phys. Rev. D* **108**, 014510 (2023).
- [59] C. S. Fischer, L. Fister, J. Luecker, and J. M. Pawłowski, *Phys. Lett. B* **732**, 273 (2014).
- [60] P. Parotto, M. Bluhm, D. Mroczek, M. Nahrgang, J. Noronha-Hostler, K. Rajagopal, C. Ratti, T. Schäfer, and M. Stephanov, *Phys. Rev. C* **101**, 034901 (2020).
- [61] J. Braun, W.-j. Fu, J. M. Pawłowski, F. Rennecke, D. Rosenblüh, and S. Yin, *Phys. Rev. D* **102**, 056010 (2020).

- [62] F. Gao and J. M. Pawłowski, *Phys. Rev. D* **105**, 094020 (2022).
- [63] Y.-r. Chen, W.-j. Fu, F. Gao, C. Huang, F. Ihssen, J. M. Pawłowski, F. Rennecke, F. R. Sattler, Y.-y. Tan, R. Wen, J. Wessely, N. Wink, and S. Yin, [arXiv:2310.19853](https://arxiv.org/abs/2310.19853).
- [64] B. J. Schaefer and M. Wagner, *Phys. Rev. D* **85**, 034027 (2012).
- [65] J. Braun *et al.* (fQCD collaboration) (2023).
- [66] T. Blum *et al.* (RBC, UKQCD Collaborations), *Phys. Rev. D* **93**, 074505 (2016).
- [67] S. Zafeiropoulos, P. Boucaud, F. De Soto, J. Rodríguez-Quintero, and J. Segovia, *Phys. Rev. Lett.* **122**, 162002 (2019).
- [68] A. K. Cyrol, L. Fister, M. Mitter, J. M. Pawłowski, and N. Strodthoff, *Phys. Rev. D* **94**, 054005 (2016).
- [69] A. K. Cyrol, M. Mitter, J. M. Pawłowski, and N. Strodthoff, *Phys. Rev. D* **97**, 054015 (2018).